

# High Purcell-enhancement in quantum-dot hybrid circular Bragg grating cavities for GHz-clockrate generation of indistinguishable photons

Lucas Rickert<sup>1,+</sup>, Daniel A. Vajner<sup>1,+</sup>, Martin von Helversen<sup>1,+</sup>, Johannes Schall<sup>1</sup>, Sven Rodt<sup>1</sup>, Stephan Reitzenstein<sup>1</sup>, Hanqing Liu<sup>2,3</sup>, Shulun Li<sup>2,3</sup>, Haiqiao Ni<sup>2,3</sup>, Zhichuan Niu<sup>2,3,\*</sup>, and Tobias Heindel<sup>1,\*</sup>

<sup>+</sup>These authors contributed equally to this work

<sup>1</sup>Institut für Festkörperphysik, Technische Universität Berlin, Hardenbergstraße 36, 10623 Berlin, Germany

<sup>2</sup>State Key Laboratory for Superlattice and Microstructures, Institute of Semiconductors, Chinese Academy of Sciences, Beijing 100083, China

<sup>3</sup>Center of Materials Science and Optoelectronics Engineering, University of Chinese Academy of Sciences, Beijing 100049, China

\*Corresponding authors: tobias.heindel@tu-berlin.de, zcnui@semi.ac.cn

August 6, 2024

## Abstract

We present Purcell-enhanced ( $F_P > 25$ ) semiconductor InAs quantum dot radiative lifetimes of  $T_1 < 30$  ps, enabled by deterministic hybrid circular Bragg gratings (hCBGs). We investigate the benefits of these short  $T_1$  times on the two-photon indistinguishability for quasi-resonant and strictly resonant excitation, and observe visibilities  $\geq 96\%$  at 12.5 ns time delay of consecutively emitted photons. The strongly Purcell-enhanced decay times enable a high degree of indistinguishability for elevated temperatures of up to 30 K, and moreover, allow for excitation of up to 1.28 GHz repetition rate. Our work highlights the prospects of high Purcell-enhanced solid-state quantum emitters for applications in quantum information and technologies operating at GHz clock-rates.

## 1 Introduction

Indistinguishable photons are a key component for implementing advanced photonic quantum information protocols. Higher-order entangled state generation enables boson sampling [1] while remote-party multi-photon interference is a prerequisite for implementation-relevant quantum key distribution (QKD) protocols, like measurement- and device-independent QKD [2]. First proof-of-concept demonstrations of device-independent QKD protocols based on indistinguishable photons from trapped atoms have been reported [3], but a significantly higher degree of scalability is expected by realizing reliable on-demand generation of indistinguishable single photons from solid-state two-level-systems [4].

While there have been several quantum emitters [5] enabling the emission of sub-Poissonian light, so-called solid-state artificial atoms formed by semiconductor quantum dots (QDs) [6], remain the only platform that simultaneously combines low multi-photon probabilities [7], emission of entangled photon pairs [8, 9], near-ideal brightness and high degrees of indistinguishability of consecutively emitted photons [10, 11, 12]. This makes them ideal candidates for applications in quantum information technologies [13]. Especially the emission of highly indistinguishable photons is a challenge,

considering that QDs are hosted in solid-state environments, which can cause significant decoherence for the generation of emitted photons due to the influences by phonons [14, 15] in the host matrix and also spectral diffusion due to charge carriers in the emitter's vicinity [16], often indicated by blinking.

Typical mitigation strategies are cooling to helium-cryogenic temperatures and external charge control [12, 17], as well as coherent excitation mechanisms [18, 19] to ensure the emission of coherent, indistinguishable photons. With these measures, remote two-photon interference has recently been demonstrated from QDs at record-high visibilities of 93% [20].

Another possibility to minimize the influence of the solid-state environment on the indistinguishability is to decrease the radiative lifetime  $T_1$  of the single-photon generating transition, which can be realized by integrating the QD into a photonic cavity and making use of the Purcell effect [21]. Reduced  $T_1$ -times increase the two-photon indistinguishability in the presence of inhomogeneous broadening [22], including dephasing from phonons [23, 24], potentially enabling operation without cost-intensive liquid-helium infrastructure.

Short  $T_1$  times are furthermore relevant when aiming to excite the QD at high excitation rates. Here,  $T_1$  should be ideally considerably shorter than the inverse repetition rate  $1/f$  (for example,  $1/f \geq 5 \cdot T_1$ ),

to avoid overlapping of subsequent pulses from following excitation circles, which would require temporal filtering leading to a reduced efficiency due to the discarding of photon events or an increased multi-photon probability. In the past, mostly electrical excitation due to fast possible excitation rates were employed for GHz-driving of In(Ga)As-QD systems, but this limited indistinguishability and a significant amount of multi-photon pulses remained, due to the non-resonant excitation condition and considerable pulse overlap [25, 26, 27, 28]. These limitations have recently been overcome in a work using coherent optical GHz excitation to generate entangled photons from a GaAs-QD [29]. However, no Purcell enhancement was employed here, but rather the faster  $T_1$ -time of this material system. Coherent GHz driving of InGaAs QDs with their inherently longer  $T_1$ -times has been elusive so far.

To enable Purcell-enhanced  $T_1$ -times suited for GHz-operation, close-to-ideal overlap between the quantum emitter and the cavity mode must be achieved both in the spatial and spectral domain, a challenge hardly mastered to date using non-deterministically fabricated QD devices and resulting in low yield [30]. Photonic cavity systems like micro-pillars [12, 31], photonic crystal cavities [32] or (hybrid) circular Bragg grating cavities (hCBGs) [33, 34, 35] require typically spatial emitter integration precision of well below 50 nm for significant Purcell enhancement.

While several QD-hCBG cavity integration methods are reported as deterministic, this often only implies that a QD is present in the fabricated cavity, but nonetheless significant deviation from theoretically possible Purcell factors is observed, generally attributed to a limited spatial integration precision. Several works have shown experimentally observed Purcell factors  $F_P$  of 3-7 [35, 36, 37, 38, 39, 40] with theoretically expected values of  $F_P \sim 20$  from simulations. The highest reported measured Purcell enhancement for QD-hCBG cavities so far are 11.7 [41] and 11.3 [30], respectively, corresponding to  $T_1$ -lifetimes of 14 ps in the former case for a GaAs-QD biexciton (XX), and 66 ps for an In(Ga)As XX.

In this work, we report the fabrication of deterministic QD-hCBG with a possible spatial integration precision of  $< 15$  nm and accuracy of  $< 20$  nm, enabling high Purcell enhancement exceeding 25, which is the highest observed Purcell enhancement in deterministically fabricated hCBG cavities reported so far, resulting in  $T_1$  of  $< 27$  ps for an InAs QD.

Exploring the impact of the high Purcell-enhancement on the quantum-optical properties of the emitted photons reveals photon-indistinguishabilities of up to 81% and 96% under p-shell and s-shell resonant excitation, respectively. Moreover, the strong Purcell enhancement results in improved temperature-robustness in two-photon interference experiments up to 30 K. Finally, we demonstrate fast coherent optical driving of the fabricated devices up to clock-rates of 1.28 GHz with minuscule effects on the multi-photon emission probability and indistinguishability.

## 2 Deterministic fabrication

A schematic of an hCBG cavity structure with embedded QD and situated on a SiO<sub>2</sub> spacer and gold back-reflector is depicted in Figure 1(a). The radius  $R$  of the hCBG's inner disc as well as a controlled variation of this parameter  $\delta R$  is indicated. Fig. 1(b) shows the influence of changes in  $\delta R$  on the simulated Purcell factor  $F_P$  based on Finite Element Method (FEM) simulations, with an expected spectral shift of maximum  $F_P$  to longer (shorter) wavelengths with larger (smaller)  $R + \delta R$  [33, 34]. The target  $R$  for the QD-hCBG cavities used in this work is  $R = 360$  nm, with a variation in  $R + \delta R$  of -20 to +30 nm shift covering a spectral range of Purcell enhancement from 885-950 nm. Purcell enhancement  $> 20$  to  $> 35$  is possible, while the reduced maximum  $F_P$  as well as the spectrally broader range of Purcell enhancement at smaller  $R + \delta R$  values stems from a reduced quality factor  $Q$  due to weaker mode confinement. Further details on the FEM simulations and hCBG parameters are given in the Supplementary Information (S.I.) S1.

The hCBG cavities are fabricated based on molecular beam epitaxy (MBE) grown InAs QDs on semi-insulating (100)-GaAs substrates using an In gradient method for low density QDs emitting between 900-940 nm [42, 43]. The QDs are embedded in a thin GaAs membrane on two separated etch stop layers and is flip-chip bonded and chemically etched to form hybrid GaAs/SiO<sub>2</sub>/Au substrates (see S.I. S2). As a next step, marker arrays are fabricated on the substrate. The deterministic QD-hCBG integration on these hybrid substrates is based on a low-temperature, marker-based cathodoluminescence (CL) [44] mapping process in an electron beam lithography (EBL) system equipped with a cryostat and a CL unit and a following EBL process (acceleration voltage  $U_B=20$  kV) at room temperature aligned to the marker arrays. Details on the deterministic fabrication can be found in S.I. S3.

A CL map with indicated QD signatures can be seen in Fig. 1(c), superimposed with the simultaneously recorded SEM image with markers before the fabrication of the hCBG cavities. The recorded map size is  $29 \times 29 \mu\text{m}^2$ . The same area with deterministically fabricated cavities is shown in Fig. 1(d). An SEM image of a fabricated cavity is shown in Fig. 1(e).

Before the integration, the QD emission patterns span several  $\mu\text{m}$  in diameter due to the large distance excited carriers can diffuse in the substrate (Fig. 1(c)). After the deterministic integration, the QD's emission is confined to the central disc of the hCBG cavity caused by the interaction with the mode and the finite interaction volume of the insulated disc on the dielectric spacer (Fig. 1(d)). We furthermore observe that the central position of the emission in the CL map after the integration only varies  $< 2$  nm, if the spectral region of the QD or of the wetting layer is selected for integration. Thus, rather than the QD-emission profile, the CL-emission map after the integration yields an accurate measure of the hCBG cavity's center position.

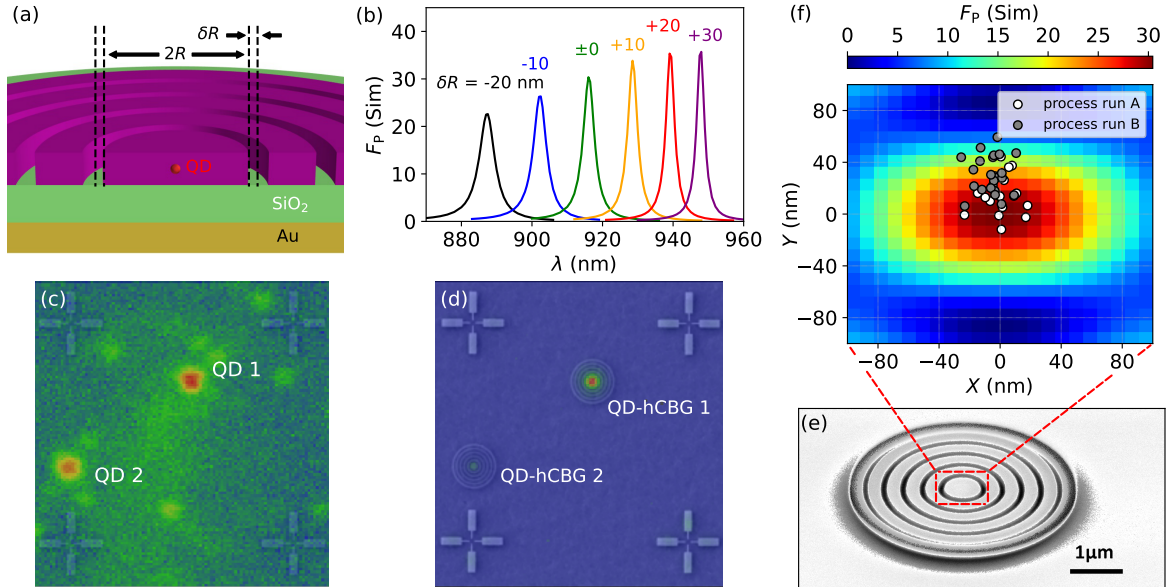


Figure 1: (a) Schematic depiction of a QD-hCBG cavity.  $R + \delta R$  represent a variation in size of the CBG's central disc. (b) FEM-simulated spectral dependency of the Purcell factor  $F_P$  of an hCBG cavity with  $\delta R$  variation. (c) Cathodoluminescence (CL-) map of a QD-containing hybrid flip-chip substrate with fabricated markers. Two QD emission patterns are indicated. (d) CL-map in (c) after the marker-aligned fabrication of hCBG cavities at the determined QD-positions. (e) Scanning Electron Microscopy (SEM) image of a fabricated QD-hCBG cavity. (f) Experimentally obtained spatial mismatch in  $x$ - and  $y$ -direction of QD- and hCBG cavity based on CL-maps before and after the integration. The simulated  $F_P$  for one of the two orthogonal polarisations is plotted as heatmap for up to  $\pm 100$  nm spatial mismatch of QD and hCBG cavity.

Therefore, comparing the QD's emission center extracted from CL maps before the fabrication with respect to the specific map's marker array to the hCBG's emission center after the fabrication to the same marker array allows for straight forward investigation of the spatial integration precision of the process. The difference between the extracted positions before and after the integration for several hCBG cavities of two exemplary processes *A* and *B* are plotted in Fig. 1(f). Alongside, the spatially-resolved maximum  $F_P$  obtained from FEM simulations for  $\delta R = 0$  nm for one of the two linear orthogonal polarisations of the hCBG mode is shown. The mean position deviation in  $x$ - and  $y$ -position for Process A (B) are  $-0.1$  nm/ $13.8$  nm ( $-6.0$  nm/ $30.4$  nm) with standard deviations of  $10.7$  nm/ $16.0$  nm ( $9.1$  nm/ $14.6$  nm). Based on these mean values and standard deviations we conclude that integration precisions  $< 15$  nm and accuracies  $< 20$  nm can be achieved with our process approach, well within the area of  $F_P > 20$ .

The obtained precision- and accuracy-values with the here presented marker-based CL technique are better than the integration performance reported in a recent systematic study that compared marker-based PL- and in-situ CL integration techniques [45]. Reasons for the superior performance of the marker-based CL approach compared to the marker-based PL-approach might be a more accurate determination of the marker positions by the electron beam, but could also originate from the marker-aligned EBL process, e.g. by the considerably higher acceleration voltages

used in Ref. [45], which might lead to lower marker contrasts during the alignment, resulting in worse alignment precision. The higher accuracy-values compared to the in situ CL integration technique, which is also carried out at cryogenic temperatures, might originate from the fact, that in case of a present temperature-induced drift during the mapping, the recording of the marker positions can compensate for this drift. It is however also important to note that the sample properties like CL emission pattern and brightness of the QDs can affect the accuracy of determining the QD's position from the CL maps, and direct comparison between the in-situ CL technique in Ref. [45] and the marker-based CL integration presented here would need to be carried out for the same sample to allow for comparison.

We point out that the mode orientation in the fabricated structures might be rotated in respect to the one shown in Fig. 1(f). The mode orientation here can be regarded as a worst-case-scenario for the observed accuracy spread of the integration. We aim to investigate and reduce the larger integration uncertainty in  $y$ -direction in the future and currently suspect a combination of residual drift and charging effects. We believe the influences of both of these factors to be more pronounced in  $y$ -direction, since the CL-maps are currently performed as  $x$ -linescans for subsequent  $y$ -pixels, meaning that neighbouring  $y$ -pixels scanned at longer times apart.

With sufficient spatial matching achieved using the marker-based CL-approach described above, we focus

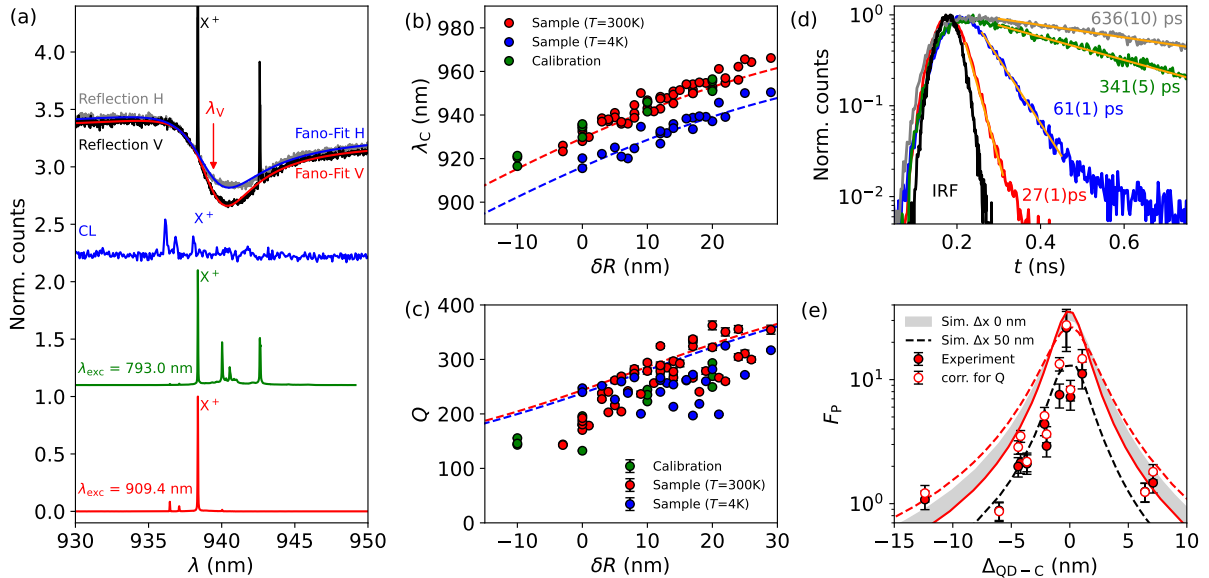


Figure 2: (a) QD-hCBG spectra obtained under white-light excitation, CL spectra before the integration and PL spectra in above-band and quasi-resonant excitation. (b) and (c) Experimental and theoretical cavity mode wavelength  $\lambda_c$  and experimental  $Q$ -factor at low and room temperature for deterministically integrated hCBGs and prior calibration process for fabricated  $\delta R$  of the hCBG. (d) Time-resolved measurements in logarithmic scale and extracted  $T_1$ -times for several  $X^+$  transitions in deterministic QD-hCBG cavities with varying spectral detuning, alongside the instrument response function (IRF). The extracted  $T_1$ -times by exponential fitting are indicated. (e) Experimental  $F_P$  values obtained from  $T_1$ -times with varying spectral detuning, as well as corrected for reduced  $Q$ -factors in the experiment. Grey shaded curves indicate theoretical  $F_P$  variations based on the influence of different  $\delta R$ -values for the investigated hCBGs, and ideal emitter position in the hCBG cavity. The black dashed line represents Purcell enhancement for an emitter that is spatially misaligned to the hCBG mode by 50 nm.

now on the spectral overlap between QD and cavity mode. Figure 2(a) shows spectrally resolved data of an exemplary QD-hCBG cavity for varying excitation methods, including the aforementioned CL-spectrum (blue), micro-photoluminescence ( $\mu$ PL)-spectra obtained under pulsed laser-excitation with two different excitation energies (green, red), and polarization-resolved reflection spectra (black) obtained by illumination with a broadband white-light-source. The  $\mu$ PL and reflection spectra were obtained by transferring the sample to a confocal  $\mu$ PL setup and cooling it to 4 K. Detailed information on the optical setup can be found in S.I. S4.

The cavity mode's spectral position can be extracted from the white-light reflection measurements by fitting the data with a Fano function [46], as indicated in red (blue) for the V- (H-)polarized cavity mode. The extracted V-polarized cavity mode wavelength  $\lambda_V$  from the Fano-fit is indicated. Apart from observing the cavity mode dips in the reflected signal, the white light is already sufficient to excite specific states of the embedded QD. The target QD emission line (the positive trion ( $X^+$ ) transition) is indicated. The second line is assigned to the neutral exciton.

The  $X^+$  emission line can also be found in the CL spectrum before the hCBG cavity fabrication (blue line in Fig. 2(a)), with additional lines blue-shifted from the trion, which we assign to higher charged states

like  $X^{2+}$  [47]. The spectra plotted in green and red show PL-spectra under above-band excitation (excitation wavelength  $\lambda_{exc}=793$  nm) and quasi-resonant excitation ( $\lambda_{exc}=909.4$  nm), respectively. We note, that for this specific wafer material, the neutral states require longer integration times and higher excitation power, to see their signatures in the CL signal, while they appear readily in the off-resonant PL-spectrum. We attribute this to the different excitation mechanisms for CL and PL, with the former exciting (positively) charged states more effectively for the present sample, which stems from the specific given doping background. We refer to Ref. [44], which also showed present positive trion signatures from CL, but with more prominent neutral states. Another indicator for noticeable positive background doping in the given sample is that photoluminescence excitation scans (see. S.I. S5) show that the  $X^+$ -state is most effectively excited under quasi-resonant conditions.

It is apparent from Fig. 2(a) that there is a small, but noticeable shift in the  $X^+$  wavelength observed from CL and PL spectra of about 1 nm. This originates from observed Stark-tuning due to charge-accumulation in the thin GaAs membrane on insulator during the CL-mapping, and can also be partly caused by the spectrometer alignment of the CL-system compared to the used PL-setup. While the influence of Stark-tuning can in the future be optimized by doped-samples sub-

strates or other means of electrical grounding, we estimate that the determination of the targeted  $X^+$  wavelength in this work is limited to  $\geq 0.5$  nm.

Since the used substrates in this work do not allow for electrical or strain tuning, the spectral QD-mode matching is fixed by the aforementioned target  $X^+$  wavelength and the hCBG cavity dimensions. However, as shown in Fig. 1(b), variations of the inner disc size allow in principle a precise setting of the hCBG's cavity mode wavelength by 1.3 nm per 1 nm  $\delta R$  variation. Fig. 2(b) shows mode wavelengths extracted from reflection measurements at room and low temperature for different variations of the central disc size, emphasizing that a 1 nm  $\delta R$  can be achieved, and is in good agreement with FEM simulations (dashed lines).

Fig. 2(c) shows the corresponding cavity  $Q$ -factor extracted from the width of the mode dip in the reflection measurements shown in (b), further confirming that the fabricated hCBGs reach the theoretically possible  $Q$  (and therefore also the expected achievable  $F_P$ ) as indicated by theory. The data points in green correspond to a fabrication process on the sample prior to the fabrication of the deterministic cavities, to confirm the assumed refractive indices and calibrate the  $\delta R$ -dependency for the sample at hand. This step is necessary, because we found that even for sample pieces from the same wafer but at different wafer-positions, the fluctuations in thickness are enough for a systematic offset of the theoretically expected mode wavelength.

Despite this initial calibration, it is however apparent that fabricated cavities with nominally identical  $\delta R$ -value show wavelength variations of up to 2 nm, and some  $Q$  factors deviate more than 20% from the theoretical  $Q$ . Furthermore, we observe a fabrication-induced polarisation-dependent mode-splitting between 0 and 3 nm due to ellipticity of the central disc. We therefore estimate the overall spectral matching accuracy to be  $\geq 1$  nm at best, if we fabricated the theory-predicted  $\delta R$ -attuned cavity on the selected QDs. In order to investigate the effect of different  $F_P$  on the quantum-optical properties, and to increase the probability of ideal spectral matching, we fabricate cavities with varying  $\delta R$  for groups of QDs with similar  $X^+$  wavelengths.

Fig. 2(d) shows time-resolved measurements of the photon arrival time distribution in semi-logarithmic scaling for spectrally filtered emission from the  $X^+$  transitions under pulsed p-shell excitation for QD-hCBGs with varying spectral detuning. The  $T_1$ -times are extracted by exponential fits, and are indicated for each curve. The  $T_1$  time without a hCBG cavity, i.e. in the surrounding membrane and therefore with a  $F_P = 1$  is determined by averaging over several  $X^+$  decays measured QDs in the surrounding membrane area under similar excitation conditions to be 680(111) ps (see. S.I. S5). The extracted  $T_1$ -times displayed in Fig. 2 correspond to experimentally measured Purcell enhancements of up to  $F_P > 25$  compared to the surrounding membrane in the case of the shortest  $T_1$  of 26.9(9) ps (red curve), which is still within the resolution of the employed superconducting nanowire de-

tector system, as indicated by the instrument response function (IRF).

The corresponding experimentally determined  $F_P$  extracted for different spectral detunings  $\Delta_{\text{QD-C}}$  between QD transition and cavity mode of each of the investigated hCBGs is shown in Fig. 1(e). The error margins of the experimentally determined  $F_P$  originate from the standard deviation of the distribution of observed planar  $T_1$  times for reference. The plotted lines depict FEM simulations for the  $F_P$ , with the shaded area in grey indicating the possible variation of  $F_P$  because of the range of different  $\delta R$ -values that were used for the cavity shift, assuming perfect spatial QD-mode matching. Since some of the cavities exhibited reduced Q-factors compared to the simulations (see Fig. 2(b)), the open circles in Fig. 2(e) show the experimentally measured  $F_P$  corrected for the reduced Q-factors, resulting in increases between 1% and 45% for better comparison to the simulated Purcell enhancement. The dashed line represents the theoretical Purcell enhancement for a spatial mismatch of  $\Delta x = 50$  nm between QD and hCBG mode. The fact, that the majority of the experimental data lies above this line indicates the high degree of spatial integration precision with the presented approach.

The achieved  $T_1$  time in this work is close to the shortest reported In(Ga)As  $T_1$  in literature in any kind of photonic resonator to-date, which, to the best of our knowledge, is 22.7 ps, achieved in a photonic crystal cavity with  $F_P$  of  $\sim 43$  [32]. We note that the target  $F_P$  of around 30 of the hCBGs presented here could readily increased to 50 and more by modifications of the dielectric spacer and grating parameters [34].

### 3 (Quasi-)resonant excitation

Before turning our focus to the influence of strong Purcell enhancement on the indistinguishability of the emitted photons by the QD-hCBG cavities with varying  $T_1$ -times, we investigate the influence of the excitation method on the quantum-optical properties. For details regarding the experimental setup to acquire the following data, including equipment and spectral filtering conditions, we refer once again to S.I. S4.

Figure 3(a) shows the emission spectrum of a QD-hCBG cavity with its  $X^+$  emission line at  $\lambda_{X^+} = 920.5$  nm under quasi-resonant excitation at  $\lambda_{\text{exc}} = 891.5$  nm at a higher QD-shell (see S.I. S5.) The corresponding time-trace and extracted  $T_1 = 54(1)$  ps ( $F_P = 12.6(2.3)$ ) for this case are shown as an inset. Besides the fast  $T_1$ -decay, the time-trace exhibits a second, slower decay of several hundred ps under these excitation conditions.

The results of time-resolved second-order-auto-correlation measurements in a Hanbury-Brown and Twiss (HBT) configuration  $g^{(2)}(t)$  under these excitation conditions can be seen in Fig. 3(b). A  $g^{(2)}(0)$ -value of 0.039(0.6) obtained from comparing the integrated peak at  $t = 0$ , to the average area of neighbouring

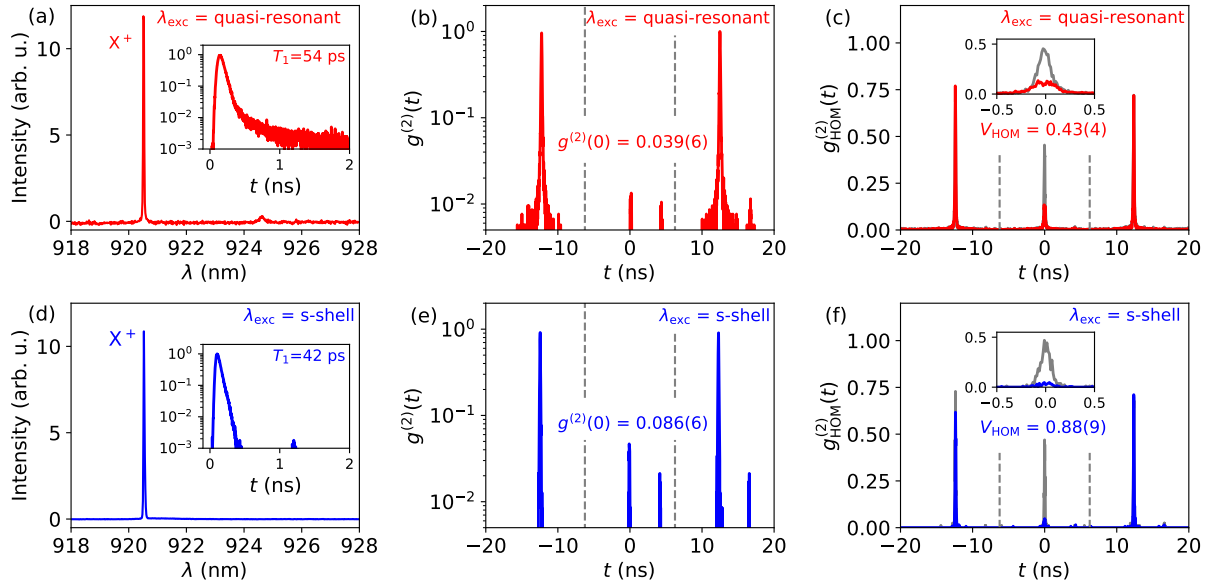


Figure 3: (a)  $\mu$ PL-spectrum of a QD-hCBG cavity under quasi-resonant excitation and corresponding time-resolved measurement as inset. (b,c) Time-resolved second-order-auto-correlation measurements in a Hanbury-Brown and Twiss (HBT) configuration  $g^{(2)}(t)$  and two-photon-interference measurements in Hong-Ou-Mandel (HOM) configuration  $g_{\text{HOM}}^{(2)}$  for emitter and conditions as in (a). (d)  $\mu$ PL-spectrum and time-resolved measurement (inset) for the same QD-hCBG cavity as in (a), but for strictly resonant (s-shell) excitation of the  $X^+$  state with a  $\pi$ -pulse. (e,f)  $g^{(2)}(t)$  and  $g_{\text{HOM}}^{(2)}$  for the same conditions as in (d).

peaks. The integration window of 12.5 ns is indicated, corresponding to the full laser repetition rate.

Two-photon-interference measurements (TPI) in Hong-Ou-Mandel (HOM) configuration  $g_{\text{HOM}}^{(2)}$  for this QD-hCBG cavity for consecutively emitted photons with a temporal delay of  $\delta t = 12.5$  ns were recorded. We estimate a spectral filtering of about 100  $\mu$ eV resulting from the employed spectrometer grating together with the spatial collection of the single-mode fiber incoupling, resulting in no filtering of the  $X^+$ 's zero phonon line (ZPL), but filtering of its phonon side band to some extent.

The  $g_{\text{HOM}}^{(2)}$ -measurement under these conditions for quasi-resonant excitation are shown in Fig. 3(c). The histograms in red and grey correspond to co-polarized and cross-polarized measurement conditions. From the peak areas around  $t=0$  ns of both measurements, a raw, i.e. uncorrected visibility of  $V_{\text{HOM}} = 1 - A_{\text{co}}/A_{\text{cross}} = 0.43(4)$  is extracted. This visibility can be corrected for the finite  $g^{(2)}(0)$  and HOM-setup limitations [20, 48] to  $V_{\text{HOM}}^{\text{corr}} \approx V_{\text{HOM}} + 2g^{(2)}(0) = 0.51(4)$ .

The identical QD-hCBG cavity can also be excited using strictly resonant excitation (s-shell) of the  $X^+$  state to achieve higher TPI-visibilitys due to higher degrees of coherence of consecutively emitted photons. The resulting spectrum for a pulse area of  $\pi$  is shown in Fig. 3(d). To filter the resonant excitation laser light, a cross-polarization configuration [49] is used.

Note that suppressing the reflected excitation laser to resonantly excite QDs in complex structures such as hCBG cavities is not straightforward due to the increased laser scattering by the photonic structure [50].

Previously, the laser suppression was enhanced by fabricating elliptical hCBG structures [51], while the devices fabricated in this work are symmetrical. Here, the necessary laser suppression is achieved by a low required excitation power due to the high hCBG incoupling efficiency, so that typical  $\pi$ -powers are of the order of 1 nW. The coherent excitation is confirmed by the observation of Rabi rotations (see S.I. S6).

The resulting time-trace for the  $X^+$  is shown in the inset. The  $T_1$  is slightly reduced to about 42 ps, and also no additional bi-exponential decay is observed in contrast to the quasi-resonant excitation conditions. This indicates that the bi-exponential decay-behaviour stems from a meta-stable decay level which is involved during the relaxation of the charge-carriers into the s-shell before recombination, since it is not observed, if the s-shell is directly populated under strictly resonant excitation.

In contrast to the aforementioned quasi-resonant excitation, the laser pulse was spectrally narrowed-down using a folded 4f pulse-shaper, which caused elongation in the time domain from about 2 ps to about 8 ps. With the temporally longer pulse compared to quasi-resonant excitation, re-excitation starts to limit the observed  $g^{(2)}(0)$ , which is 0.086(6) under RF excitation, as is shown in Fig. 3(e). Another factor that limits the achievable  $g^{(2)}(0)$  is insufficient laser suppression, because of scattered resonant laser light scattered by the hCBG cavity, limiting the effectiveness of the spatial suppression pattern.

Despite the noticeable multi-photon events, the raw indistinguishability under RF excitation is vastly improved compared to quasi-resonant excitation. The re-

spective  $g_{\text{HOM}}^{(2)}$ -measurement is shown in Fig. 3(f). The extracted raw visibility is  $V_{\text{HOM}} = 0.88(9)$ , obtained by integrating again over the full laser repetition period. We point out, that using  $V_{\text{HOM}} + 2g^{(2)}(0)$  as correction would yield an unrealistic corrected visibility greater than unity. Previous work [52] showed that different potential causes of elevated  $g^{(2)}(0)$ -values have to be taken into account for visibility correction - with e.g. the effects of stray laser light being more accurately described by a correction of  $V_{\text{HOM}}^{\text{corr}} = V_{\text{HOM}} + Bg^{(2)}(0)$  using a factor  $1 \leq B \leq 2$ . A conservative visibility correction using  $B = 1$  yields a corrected HOM visibility under RF excitation of  $V_{\text{HOM}}^{\text{corr}} \geq 0.96$  for the measurement in Fig. 3. This value is among the highest reported indistinguishabilities at this time delay and RF excitation for In(Ga)As QDs at these wavelengths in literature [10, 11, 12, 32]. This is even more noteworthy, since the employed QD-hCBG devices in this present work have no active control of the charge environment, and the observed indistinguishability is therefore expected to be still decreased due to charge fluctuation in the QD's vicinity.

We further point out that both the  $g^{(2)}(t)$  and  $g_{\text{HOM}}^{(2)}(t)$  measurements shown in Fig. 3 exhibit small amounts of signal from a back-reflection towards the detection system most likely caused at a fiber-to-fiber mating. This is especially apparent in Fig. 3(e) but also visible in the inset of Fig. 3(d). All obtained  $g^{(2)}(0)$  and  $V_{\text{HOM}}$  are not corrected for that, i.e. no temporal filtering has been applied.

Besides the very high growth-quality of the employed substrates, we attribute the observed high indistinguishability to the strong Purcell enhancement, and short  $T_1$  time. We will investigate the influence of varying  $T_1$ -times on the indistinguishability in the following.

## 4 $T_1$ influence on $V_{\text{HOM}}$

Extracted TPI visibilities for varying  $T_1$  times are displayed in Figure 4(a), for p-shell and s-shell excitation of the specific QD-hCBG system. Note that all the measurements were taken with the identical degree of spectral filtering via a monochromator and following single mode fiber in-coupling, as described above. Both the raw and corrected extracted visibilities (latter with  $B = 2$  for p-shell and  $B = 1$  for s-shell, see above) are plotted. The error bars correspond to the measured  $B \cdot g^{(2)}(0)$ -values for the specific QD-hCBGs. The dashed lines are  $T_1$ -dependent theoretical visibilities based on equation (1) [22].

$$V_{\text{HOM}}(T_1, \Gamma) = \frac{A(\Gamma)}{T_1} \exp\left(\frac{A(\Gamma)^2}{\pi T_1^2}\right) \cdot \text{erfc}\left(\frac{A(\Gamma)}{T_1 \pi}\right) \quad (1)$$

with the error-function  $\text{erfc}()$  and the factor  $A = \sqrt{\log 2} / \sqrt{2\pi\Gamma}$ , including the inhomogeneously broadened QD emission line following a Gaussian distribution with linewidth  $\Gamma$ .

The beneficial effect of strong Purcell enhancement on the HOM visibility is apparent for both kinds of excitation mechanisms, with highest visibility values of  $V_{\text{HOM}} = 0.75(6)$  ( $V_{\text{HOM}}^{\text{corr}} = 0.81(6)$ ) for a QD-hCBG with  $T_1 = 26.9(9)$  ps under p-shell excitation and the aforementioned  $V_{\text{HOM}} = 0.88(9)$  ( $V_{\text{HOM}}^{\text{corr}} = 0.96(9)$ ) for a QD-hCBG with  $T_1 = 41.7(2)$  ps under resonant excitation. Additionally, the strongly reduced inhomogeneous broadening under RF excitation compared to quasi-resonant excitation is apparent from comparison to theory, and visibilities of  $> 80\%$  are still observed even for comparably long  $T_1$ -times of 400 ps ( $F_P \approx 1.7$ ) under resonant excitation.

To get additional information on the coherence properties of the interfered photons, we extracted  $T_2$ -coherence times from the central dip in the co-polarized HOM-measurement via an exponential fit, since the width of the dip is related to the coherence time [53]. Fig. 4(c) shows the  $T_1$ -resolved  $T_2$ -times for the investigated QD-hCBG cavities in (a). The dashed grey line corresponds to a Fourier-limited  $2T_2 = T_1$  relation.

It is apparent from the data in Fig. 4(c) that for the cases of significant Purcell enhancement, the observed  $T_1$  and  $T_2$  times are getting close to this relation even for quasi-resonant excitation, which in turn results in the observed high TPI visibilities. The  $T_2$  times extracted for RF excitation are significantly higher, so that the reduction in  $T_1$  is already sufficient for close to Fourier-limited photons at moderate  $F_P$ . We point out here that for the data points in Fig. 4 with very high visibility, it was not possible to extract  $T_2$  from the co-polarized measurement, because the present multiphoton events mask the dip. However, the comparison clearly indicates that the investigated indistinguishability improvement can be related to shortened  $T_1$ -times, which renders the emitted photons more resilient to present decoherence during the charge-carrier recombination after excitation.

This increased indistinguishability in the presence of decoherence for shortened  $T_1$  times is also beneficial, if this decoherence is caused by further inhomogeneous broadening due to phonon interaction [23, 24, 54]. Fig. 4(d) shows extracted TPI visibilities under p-shell excitation for varying degrees of Purcell-enhancement in the temperature range of  $\sim 5 - 45$  K. The dotted lines are theoretical TPI visibilities according to

$$V_{\text{HOM}}(T, \Gamma) = V_{\text{HOM}}(T_1, \Gamma) \frac{\gamma}{\gamma + \gamma^*(T)} \quad (2)$$

where  $V_{\text{HOM}}(\Gamma)$  corresponds to equation (1) and accounts for given dephasing due to the quasi-resonant excitation at given  $T_1$  and  $\Gamma$ , and the second factor assumes Markovian-dynamics for the indistinguishability [14, 23, 24]. Here,  $\gamma$  represents the Fourier-limited linewidth  $\gamma = \hbar/T_1$  and  $\gamma^*(T)$  being the broadening of the ZPL due to dephasing by scattering from thermal acoustic photons [24]. According to Ref. [24] we approximate  $\gamma^*(T) = \alpha n(E)(n(E) + 1)$  with  $n(E)$  being the Bose-Einstein function. For the curves in Fig. 4,  $\alpha$  is set to  $3 \mu\text{eV}$  and  $E$  to  $1 \text{ meV}$ , similar to previous works [24]. The corresponding  $\Gamma$ -values for each

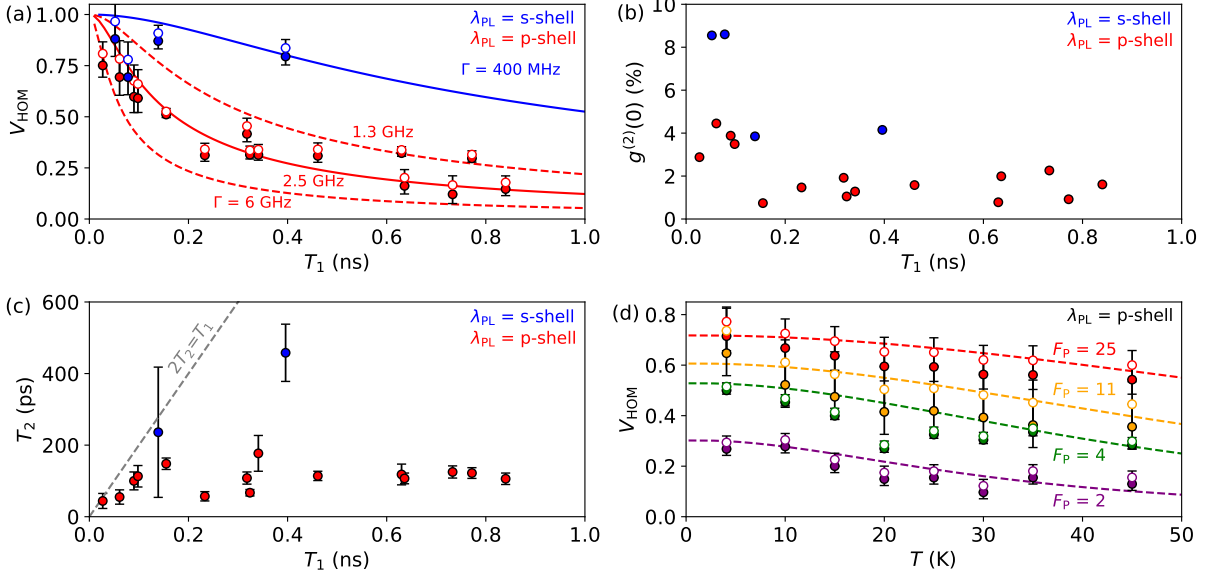


Figure 4: (a) Measured raw  $V_{\text{HOM}}$  (filled circles) and corrected  $V_{\text{HOM}}^{\text{corr}}$  (open circles) for varying  $X^+$   $T_1$  times under p-shell and s-shell excitation. The plotted theory curves are according to equation (1) with respective  $\Gamma$ -values. (b) Corresponding  $g^{(2)}(0)$ -values for the data in (a). (c) Corresponding  $T_2$ -time extracted from fits of the central HOM-dip for the data in (a). (d) Measured raw  $V_{\text{HOM}}$  (filled circles) and corrected  $V_{\text{HOM}}^{\text{corr}}$  (open circles) for varying  $X^+$  transitions with varying  $F_P$  under p-shell excitation. The plotted theory curves are according to equation (2).

curve at given  $F_P$  are between 2.5 and 6 GHz, as obtained by comparison of experimental data and theory in Fig. 4(a).

Fig. 4(d) shows clearly the beneficial effect of strong Purcell enhancement on the photon indistinguishability for elevated temperatures, with still  $V_{\text{HOM}}^{\text{corr}} > 60\%$  at  $T = 30 - 40$  K for  $F_P = 25$ . This temperature is interesting from a technological point-of-view, since it is reachable with compact Stirling cryocoolers, operable without the need of liquid helium cooling [55, 56, 57].

We furthermore point out that changes in  $T_1$  due to the temperature induced tuning of the  $X^+$ -emission wavelength as well as the hCBG cavity mode also affect the obtained indistinguishabilities. For example, the QD with  $F_P = 25$  showed  $T_1 < 30$  ps at  $T = 5$  K, and  $T_1 = 45$  ps at  $T = 45$  K, reducing  $V_{\text{HOM}}(T_1, \Gamma)$  from 0.76 to 0.64. The reduction of temperature influence on the indistinguishability at these high  $F_P$  is therefore expected to be even higher than what can be seen in Fig. 4, and could be accessed if the QD-hCBG-mode matching could be restored independently from temperature, as was done in previous works e.g. via Stark-tuning [24]. On the other hand, it is worth noting that the spectrally broad Purcell enhancement of hCBG cavities can act as a stabilizing element for temperature shifts, as indicated here by maintaining comparably high indistinguishability values due to low changes in  $T_1$  also in the absence of independent tuning possibilities.

## 5 GHz operation

Finally, we demonstrate that the high Purcell enhancement achieved in this work allows for increasing the excitation laser repetition rate into the GHz range. Since we do not have a pulsed excitation laser with repetition rates  $> 80$  MHz available, we multiply our 80 MHz pulsed laser signal in a self-built sequential rate-doubling setup up to 16-fold, resulting in an excitation pulse separation of  $\sim 781$  ps or 1.28 GHz excitation rate. Details on the rate multiplication setup can be found in S.I. S7. Figure 5 shows quantum-optical performances with this GHz rate excitation, for the same QD-hCBG cavity with  $T_1$  of 40-50 ps used for the measurements in Fig. 3 at 80 MHz. The  $T_1$  time of this QD-hCBG cavity is therefore  $> 15 \cdot 1/f$ .

Fig. 5(a) shows time traces under p-shell and s-shell excitation conditions for this GHz rate. As can be seen, due to the strongly reduced  $T_1$ -time, the successive peaks are well separated, despite the slower bi-exponential decay component present under quasi-resonant excitation, as discussed previously.

Fig. 5(b) and (c) show a corresponding  $g^{(2)}(t)$  and  $g_{\text{HOM}}^{(2)}(t)$  measurement under p-shell excitation, yielding  $g^{(2)}(0) = 0.05(1)$  and  $V_{\text{HOM}} = 0.66(5)$  ( $V_{\text{HOM}}^{\text{corr}} = 0.76(5)$ ) from integrating co-and-cross polarized data over time-windows of 0.781 ns equal to the repetition rate. Comparison to Fig. 3(a) and (b) shows, that these values at 1.28 GHz excitation rate are nearly identical to driving the QD-hCBG cavity system under 80 MHz excitation rates, therefore confirming that the strong Purcell enhancement enables GHz rate op-



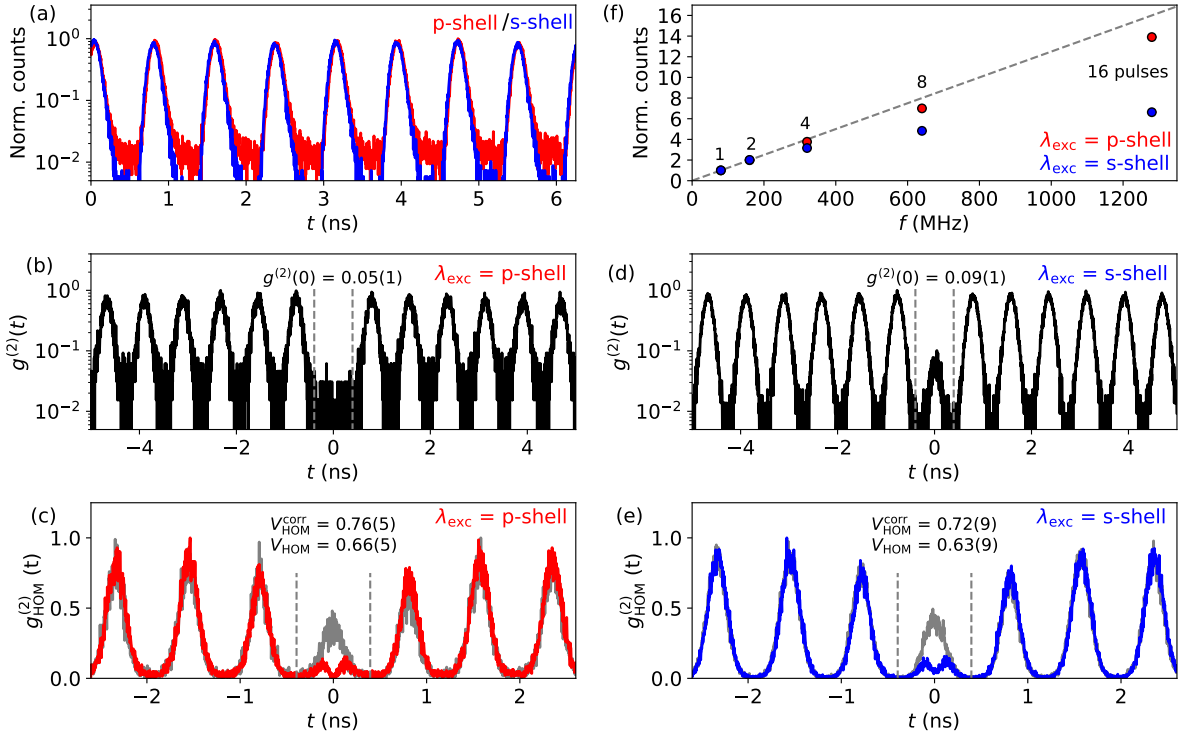


Figure 5: (a) Time-resolved measurements of a QD-hCBGs cavity with  $T_1 < 50$  ps under p-shell and s-shell excitation at 1.28 GHz repetition rate. (b) Second-order auto-correlation  $g^{(2)}(t)$ -measurement and (c) Two-photon interference  $g_{\text{HOM}}^{(2)}(t)$  at 1.28 GHz p-shell excitation for the QD-hCBG cavity in (a). (d) Second-order auto-correlation  $g^{(2)}(t)$ -measurement and (e) Two-photon interference  $g_{\text{HOM}}^{(2)}(t)$  at 1.28 GHz under  $\pi$ -pulse s-shell excitation for the QD-hCBG cavity in (a). (f) Measured count-rates for an increasing number of excitation pulses (and correspondingly higher excitation rate  $f$ ), normalized by the 1-pulse result for p-shell (red) and s-shell (blue) excitation.

eration without any detrimental effect on the quantum-optical properties for quasi-resonant excitation.

Fig. 5(d) and (e) show  $g^{(2)}(t)$  and  $g_{\text{HOM}}^{(2)}(t)$  measurements under s-shell 1.28 GHz excitation. While the  $g^{(2)}(0)$ -value of 0.09(1) is in accordance with the observed 80 MHz value, taking re-excitation and imperfect laser-suppression into account, the observed HOM indistinguishability was surprisingly limited: A raw indistinguishability of  $V_{\text{HOM}} = 0.63(5)$  ( $V_{\text{HOM}}^{\text{corr}} = 0.72(5)$ ) was observed, even lower than for the p-shell quasi-resonant excitation. To confirm that the reason is indeed the GHz excitation, we blocked the respective additional excitation pulses while keeping all other conditions (alignment, excitation wavelength, power, filtering) unchanged, and measured the indistinguishability again under 80 MHz s-shell excitation, recovering the  $> 0.95$ -values observed before and described above. We therefore suspect that the increased excitation rate is the cause for the limited  $V_{\text{HOM}}$  in strictly-resonant excitation.

A further indicator for this is the observed count-rate for different excitation rates, which is shown in Fig. 5(f). The grey dashed line indicates the expected linear increase in count-rate with pulse number multiplication from 80 MHz (1 pulse) to 1.28 GHz (16 pulses). As can be seen, under s-shell excitation (blue dots), the observed count-rate starts to deviate from

the expected linear behaviour for  $f > 300$  MHz (4 pulses, 3.125 ns time window), and reaches only about 25 % of the expected count-rate at 1.28 GHz or 16 pulses in the 12.5 ns time window. The p-shell GHz excitation (red dots) also shows slightly lower count-rates than the 16-times multiplication, but is much closer to the expected values.

We suspect this saturation behaviour and the reduced indistinguishability to be linked to the availability of holes to form the  $X^+$  ground state. Since the observed time-resolved emission properties, i.e.  $T_1$ -times do not appear to be influenced by the excitation rate, we suspect that the charge carrier creation prior to the emission is the limiting factor. More concretely, that at excitation rates above 300 MHz, the available time to make additional holes available to keep forming  $X^+$ -states by optical excitation is too short, limiting the achievable count-rate.

Likewise, the detrimental effects of high excitation rates on the indistinguishability in s-shell excitation could be explained by the changing charge-environment due to the non-equilibrium conditions for the required excess holes at high excitation rates. Quasi-resonant p-shell excitation on the other hand is energetically above possible hole-states, and might still provide enough additional holes per pulse to limit the

effects on the charge-environment at high rates, without influencing the charge environment substantially.

## 6 Discussion

In summary, we presented deterministically fabricated QD-hCBG devices with sufficient spatial and spectral matching to achieve Purcell enhancements of up to  $F_P > 25$  for a  $X^+$  state tuned to the cavity mode, which is the closest value to the expected theoretical performance of these cavities reported so far. We demonstrated the beneficial effects of these strongly reduced  $T_1$  times for the generation of indistinguishable photons both for strictly resonant as well as quasi-resonant excitation conditions, and also for application-relevant temperature ranges of  $\geq 30$  K. Moreover, the achieved  $T_1$ -times  $< 50$  ps enabled excitation rates well beyond the usual 80 MHz driving, with up to 1.28 GHz used in this work, currently just limited by the experimentally achievable excitation rates. While quasi-resonant excitation at these high rates did show no deterioration in the quantum-optical properties, higher excitation rates did show a slight detrimental effect on the two photon indistinguishability for strictly resonant excitation wavelengths. Note however, that this behavior is presumably linked to the type of charged state investigated here and its specific environment and intrinsic doping. Generally speaking, RF should be best suited for GHz excitation rates, since it offers the shortest achievable  $T_1$ -time.

In order to investigate the origins for this behaviour, further work is needed, considering that very few works have achieved device performances that allow for resonant (optical) GHz driving rates and taking a closer look at the associated emerging physics. Since we suspect charge-carrier mechanics to be limiting the current GHz indistinguishability, means of charge control in the form of gated [58, 59, 60] hCBG cavities appear beneficial to understand and overcome this limitation. Our fabrication method is straight-forwardly compatible for such substrates, which would also allow for means of QD-cavity mode matching at elevated temperatures, by tuning the QD emission line back into resonance. First results on photonic ring structures with gated contacts have been recently reported [61], although without Purcell enhancement so far.

Since indistinguishabilities close to 0.8 at quasi-resonant wavelengths were already reached here with the Purcell factors achieved in this work, adapted designs could push these values even further, since optimization of the layer structure and CBG dimensions can readily provide Purcell enhancements which are a factor of 2 or 3 higher [34]. While the associated increased Q-factors would tighten the requirements for spectral QD-mode matching, they would also be beneficial for increasing the indistinguishability and efficiency of the cavities at elevated temperatures [23] by reducing the amount of photons not emitted into the ZPL.

Lastly, the indistinguishability of currently extensively investigated telecom-QDs [37, 38] with so far limited integration accuracy and therefore limited Purcell enhancement would benefit greatly from the high precision integration techniques for spatial and spectral mode matching as shown here.

## 7 Data and Code Availability

The Data obtained in this work can be provided by the authors upon reasonable request.

## 8 Funding

The authors acknowledge financial support by the German Federal Ministry of Education and Research (BMBF) via the project “QuSecure” (Grant No. 13N14876) within the funding program Photonic Research Germany, the BMBF joint project “tubLAN Q.0” (Grant No. 16KISQ087K), and by the Einstein Foundation Berlin via the Einstein Research Unit “Quantum Devices”. H.L., S.L., H.N., and Z.N. further acknowledge funding by the National Key Technology R&D program of China (Grant No. 2018YFA0306101) and J.H., S.Rodt, and S.Reitzenstein by the German Federal Ministry of Education and Research (BMBF) through the project QR.X Quantenrepeater.Link (Funding ID 16KISQ014) and German Research Foundation via project INST 131/795-1 FUGG.

## 9 Disclosure

The authors declare no conflict of interest.

## References

- [1] S. Aaronson and A. Arkhipov, “The computational complexity of linear optics,” in *Proceedings of the forty-third annual ACM symposium on Theory of computing*, (San Jose California USA), pp. 333–342, ACM, June 2011.
- [2] V. Zapatero, T. Van Leent, R. Arnon-Friedman, W.-Z. Liu, Q. Zhang, H. Weinfurter, and M. Curty, “Advances in device-independent quantum key distribution,” *npj Quantum Information*, vol. 9, p. 10, Feb. 2023.
- [3] W. Zhang, T. Van Leent, K. Redeker, R. Garthoff, R. Schwonnek, F. Fertig, S. Eppelt, W. Rosenfeld, V. Scarani, C. C.-W. Lim, and H. Weinfurter, “A device-independent quantum key distribution system for distant users,” *Nature*, vol. 607, pp. 687–691, July 2022.
- [4] S. Rodt, S. Reitzenstein, and T. Heindel, “Deterministically fabricated solid-state quantum-light sources,” *Journal of Physics: Condensed Matter*, vol. 32, p. 153003, Apr. 2020.

- [5] I. Aharonovich, D. Englund, and M. Toth, “Solid-state single-photon emitters,” *Nature Photonics*, vol. 10, pp. 631–641, Oct. 2016.
- [6] D. A. Vajner, L. Rickert, T. Gao, K. Kaymazlar, and T. Heindel, “Quantum Communication Using Semiconductor Quantum Dots,” *Advanced Quantum Technologies*, vol. 5, p. 2100116, July 2022.
- [7] L. Schweickert, K. D. Jöns, K. D. Zeuner, S. F. Covre Da Silva, H. Huang, T. Lettner, M. Reindl, J. Zichi, R. Trotta, A. Rastelli, and V. Zwiller, “On-demand generation of background-free single photons from a solid-state source,” *Applied Physics Letters*, vol. 112, p. 093106, Feb. 2018.
- [8] O. Benson, C. Santori, M. Pelton, and Y. Yamamoto, “Regulated and Entangled Photons from a Single Quantum Dot,” *Physical Review Letters*, vol. 84, pp. 2513–2516, Mar. 2000.
- [9] N. Akopian, N. H. Lindner, E. Poem, Y. Berlatzky, J. Avron, D. Gershoni, B. D. Gerardot, and P. M. Petroff, “Entangled Photon Pairs from Semiconductor Quantum Dots,” *Physical Review Letters*, vol. 96, p. 130501, Apr. 2006.
- [10] X. Ding, Y.-P. Guo, M.-C. Xu, R.-Z. Liu, G.-Y. Zou, J.-Y. Zhao, Z.-X. Ge, Q.-H. Zhang, H.-L. Liu, L.-J. Wang, M.-C. Chen, H. Wang, Y.-M. He, Y.-H. Huo, C.-Y. Lu, and J.-W. Pan, “High-efficiency single-photon source above the loss-tolerant threshold for efficient linear optical quantum computing,” Nov. 2023. arXiv:2311.08347 [quant-ph].
- [11] N. Tamm, A. Javadi, N. O. Antoniadis, D. Najer, M. C. Löbl, A. R. Korsch, R. Schott, S. R. Valentin, A. D. Wieck, A. Ludwig, and R. J. Warburton, “A bright and fast source of coherent single photons,” *Nature Nanotechnology*, vol. 16, pp. 399–403, Apr. 2021.
- [12] N. Somaschi, V. Giesz, L. De Santis, J. C. Loredó, M. P. Almeida, G. Hornecker, S. L. Portalupi, T. Grange, C. Antón, J. Demory, C. Gómez, I. Sagnes, N. D. Lanzillotti-Kimura, A. Lemaître, A. Auffèves, A. G. White, L. Lanco, and P. Senellart, “Near-optimal single-photon sources in the solid state,” *Nature Photonics*, vol. 10, pp. 340–345, May 2016.
- [13] T. Heindel, J.-H. Kim, N. Gregersen, A. Rastelli, and S. Reitzenstein, “Quantum dots for photonic quantum information technology,” *Advances in Optics and Photonics*, vol. 15, p. 613, Sept. 2023.
- [14] J. Bylander, I. Robert-Philip, and I. Abram, “Interference and correlation of two independent photons,” *The European Physical Journal D*, vol. 22, pp. 295–301, Feb. 2003.
- [15] E. V. Denning, J. Iles-Smith, N. Gregersen, and J. Mork, “Phonon effects in quantum dot single-photon sources,” *Optical Materials Express*, vol. 10, p. 222, Jan. 2020.
- [16] J. Liu, K. Konthasinghe, M. Davanço, J. Lawall, V. Anant, V. Verma, R. Mirin, S. W. Nam, J. D. Song, B. Ma, Z. S. Chen, H. Q. Ni, Z. C. Niu, and K. Srinivasan, “Single Self-Assembled InAs / GaAs Quantum Dots in Photonic Nanostructures: The Role of Nanofabrication,” *Physical Review Applied*, vol. 9, p. 064019, June 2018.
- [17] L. Zhai, M. C. Löbl, G. N. Nguyen, J. Ritzmann, A. Javadi, C. Spinnler, A. D. Wieck, A. Ludwig, and R. J. Warburton, “Low-noise GaAs quantum dots for quantum photonics,” *Nature Communications*, vol. 11, p. 4745, Sept. 2020.
- [18] A. Müller, E. B. Flagg, P. Bianucci, X. Y. Wang, D. G. Deppe, W. Ma, J. Zhang, G. J. Salamo, M. Xiao, and C. K. Shih, “Resonance Fluorescence from a Coherently Driven Semiconductor Quantum Dot in a Cavity,” *Physical Review Letters*, vol. 99, p. 187402, Nov. 2007.
- [19] S. Ates, S. M. Ulrich, S. Reitzenstein, A. Löffler, A. Forchel, and P. Michler, “Post-Selected Indistinguishable Photons from the Resonance Fluorescence of a Single Quantum Dot in a Microcavity,” *Physical Review Letters*, vol. 103, p. 167402, Oct. 2009.
- [20] L. Zhai, G. N. Nguyen, C. Spinnler, J. Ritzmann, M. C. Löbl, A. D. Wieck, A. Ludwig, A. Javadi, and R. J. Warburton, “Quantum interference of identical photons from remote GaAs quantum dots,” *Nature Nanotechnology*, vol. 17, pp. 829–833, Aug. 2022.
- [21] Purcell, E. M., “B10. Spontaneous Emission Probabilities at Radio Frequencies.,” *Physical Review*, vol. 69, p. 681, June 1946.
- [22] P. Gold, A. Thoma, S. Maier, S. Reitzenstein, C. Schneider, S. Höfling, and M. Kamp, “Two-photon interference from remote quantum dots with inhomogeneously broadened linewidths,” *Physical Review B*, vol. 89, p. 035313, Jan. 2014.
- [23] T. Grange, G. Hornecker, D. Hunger, J.-P. Poizat, J.-M. Gérard, P. Senellart, and A. Auffèves, “Cavity-Funneled Generation of Indistinguishable Single Photons from Strongly Dissipative Quantum Emitters,” *Physical Review Letters*, vol. 114, p. 193601, May 2015.
- [24] T. Grange, N. Somaschi, C. Antón, L. De Santis, G. Coppola, V. Giesz, A. Lemaître, I. Sagnes, A. Auffèves, and P. Senellart, “Reducing Phonon-Induced Decoherence in Solid-State Single-Photon Sources with Cavity Quantum Electrodynamics,” *Physical Review Letters*, vol. 118, p. 253602, June 2017.

- [25] F. Hargart, C. A. Kessler, T. Schwarzbäck, E. Koroknay, S. Weidenfeld, M. Jetter, and P. Michler, “Electrically driven quantum dot single-photon source at 2 GHz excitation repetition rate with ultra-low emission time jitter,” *Applied Physics Letters*, vol. 102, p. 011126, Jan. 2013.
- [26] A. Schlehahn, A. Thoma, P. Munnely, M. Kamp, S. Höfling, T. Heindel, C. Schneider, and S. Reitzenstein, “An electrically driven cavity-enhanced source of indistinguishable photons with 61% overall efficiency,” *APL Photonics*, vol. 1, p. 011301, Apr. 2016.
- [27] M. Anderson, T. Müller, J. Skiba-Szymanska, A. B. Krysa, J. Huwer, R. M. Stevenson, J. Heffernan, D. A. Ritchie, and A. J. Shields, “Gigahertz-Clocked Teleportation of Time-Bin Qubits with a Quantum Dot in the Telecommunication C Band,” *Physical Review Applied*, vol. 13, p. 054052, May 2020.
- [28] G. Shooter, Z.-H. Xiang, J. R. A. Müller, J. Skiba-Szymanska, J. Huwer, J. Griffiths, T. Mitchell, M. Anderson, T. Müller, A. B. Krysa, R. Mark Stevenson, J. Heffernan, D. A. Ritchie, and A. J. Shields, “1GHz clocked distribution of electrically generated entangled photon pairs,” *Optics Express*, vol. 28, p. 36838, Nov. 2020.
- [29] C. Hopfmann, W. Nie, N. L. Sharma, C. Weigelt, F. Ding, and O. G. Schmidt, “Maximally entangled and gigahertz-clocked on-demand photon pair source,” *Physical Review B*, vol. 103, p. 075413, Feb. 2021.
- [30] H. Wang, H. Hu, T.-H. Chung, J. Qin, X. Yang, J.-P. Li, R.-Z. Liu, H.-S. Zhong, Y.-M. He, X. Ding, Y.-H. Deng, Q. Dai, Y.-H. Huo, S. Höfling, C.-Y. Lu, and J.-W. Pan, “On-Demand Semiconductor Source of Entangled Photons Which Simultaneously Has High Fidelity, Efficiency, and Indistinguishability,” *Physical Review Letters*, vol. 122, p. 113602, Mar. 2019.
- [31] X. Ding, Y. He, Z.-C. Duan, N. Gregersen, M.-C. Chen, S. Unsleber, S. Maier, C. Schneider, M. Kamp, S. Höfling, C.-Y. Lu, and J.-W. Pan, “On-Demand Single Photons with High Extraction Efficiency and Near-Unity Indistinguishability from a Resonantly Driven Quantum Dot in a Micropillar,” *Physical Review Letters*, vol. 116, p. 020401, Jan. 2016.
- [32] F. Liu, A. J. Brash, J. O’Hara, L. M. P. P. Martins, C. L. Phillips, R. J. Coles, B. Royall, E. Clarke, C. Bentham, N. Prtljaga, I. E. Itskevich, L. R. Wilson, M. S. Skolnick, and A. M. Fox, “High Purcell factor generation of indistinguishable on-chip single photons,” *Nature Nanotechnology*, vol. 13, pp. 835–840, Sept. 2018.
- [33] B. Yao, R. Su, Y. Wei, Z. Liu, T. Zhao, and J. Liu, “Design for Hybrid Circular Bragg Gratings for a Highly Efficient Quantum-Dot Single-Photon Source,” *Journal of the Korean Physical Society*, vol. 73, pp. 1502–1505, Nov. 2018.
- [34] L. Rickert, T. Kupko, S. Rodt, S. Reitzenstein, and T. Heindel, “Optimized designs for telecom-wavelength quantum light sources based on hybrid circular Bragg gratings,” *Optics Express*, vol. 27, p. 36824, Dec. 2019.
- [35] J. Liu, R. Su, Y. Wei, B. Yao, S. F. C. D. Silva, Y. Yu, J. Iles-Smith, K. Srinivasan, A. Rastelli, J. Li, and X. Wang, “A solid-state source of strongly entangled photon pairs with high brightness and indistinguishability,” *Nature Nanotechnology*, vol. 14, pp. 586–593, June 2019.
- [36] S. Kolatschek, C. Nawrath, S. Bauer, J. Huang, J. Fischer, R. Sittig, M. Jetter, S. L. Portalupi, and P. Michler, “Bright Purcell Enhanced Single-Photon Source in the Telecom O-Band Based on a Quantum Dot in a Circular Bragg Grating,” *Nano Letters*, vol. 21, pp. 7740–7745, Sept. 2021.
- [37] C. Nawrath, R. Joos, S. Kolatschek, S. Bauer, P. Pruy, F. Hornung, J. Fischer, J. Huang, P. Vijayan, R. Sittig, M. Jetter, S. L. Portalupi, and P. Michler, “Bright Source of Purcell-Enhanced, Triggered, Single Photons in the Telecom C-Band,” *Advanced Quantum Technologies*, vol. 6, p. 2300111, Nov. 2023.
- [38] P. Holewa, D. A. Vajner, E. Zięba-Ostójk, M. Wasiluk, B. Gaál, A. Sakanas, M. Burakowski, P. Mrowiński, B. Krajnik, M. Xiong, K. Yvind, N. Gregersen, A. Musiał, A. Huck, T. Heindel, M. Syperek, and E. Semenova, “High-throughput quantum photonic devices emitting indistinguishable photons in the telecom C-band,” *Nature Communications*, vol. 15, p. 3358, Apr. 2024.
- [39] A. Barbiero, J. Huwer, J. Skiba-Szymanska, D. J. P. Ellis, R. M. Stevenson, T. Müller, G. Shooter, L. E. Goff, D. A. Ritchie, and A. J. Shields, “High-Performance Single-Photon Sources at Telecom Wavelength Based on Broadband Hybrid Circular Bragg Gratings,” *ACS Photonics*, vol. 9, pp. 3060–3066, Sept. 2022.
- [40] J. Kaupp, Y. Reum, F. Kohr, J. Michl, Q. Buchinger, A. Wolf, G. Peniakov, T. Huber-Loyola, A. Pfenning, and S. Höfling, “Purcell-Enhanced Single-Photon Emission in the Telecom C-Band,” *Advanced Quantum Technologies*, vol. 6, p. 2300242, Dec. 2023.
- [41] M. B. Rota, T. M. Krieger, Q. Buchinger, M. Beccaceci, J. Neuwirth, H. Huet, N. Horová, G. Lovicu, G. Ronco, S. F. Covre Da Silva, G. Pettinari, M. Moczala-Dusanowska, C. Kohlberger, S. Manna, S. Stroj, J. Freund, X. Yuan, C. Schneider, M. Ježek, S. Höfling, F. Basso Basset,

- T. Huber-Loyola, A. Rastelli, and R. Trotta, “A source of entangled photons based on a cavity-enhanced and strain-tuned GaAs quantum dot,” *eLight*, vol. 4, p. 13, Dec. 2024.
- [42] X.-J. Shang, J.-X. Xu, B. Ma, Z.-S. Chen, S.-H. Wei, M.-F. Li, G.-W. Zha, L.-C. Zhang, Y. Yu, H.-Q. Ni, and Z.-C. Niu, “Proper In deposition amount for on-demand epitaxy of InAs/GaAs single quantum dots,” *Chinese Physics B*, vol. 25, p. 107805, Oct. 2016.
- [43] Z.-S. Chen, B. Ma, X.-J. Shang, Y. He, L.-C. Zhang, H.-Q. Ni, J.-L. Wang, and Z.-C. Niu, “Telecommunication Wavelength-Band Single-Photon Emission from Single Large InAs Quantum Dots Nucleated on Low-Density Seed Quantum Dots,” *Nanoscale Research Letters*, vol. 11, p. 382, Dec. 2016.
- [44] S. Rodt, A. Schliwa, K. Pötschke, F. Guffarth, and D. Bimberg, “Correlation of structural and few-particle properties of self-organized InAs/GaAs quantum dots,” *Physical Review B*, vol. 71, p. 155325, Apr. 2005.
- [45] A. A. Madigawa, J. N. Donges, B. Gaál, S. Li, M. A. Jacobsen, H. Liu, D. Dai, X. Su, X. Shang, H. Ni, J. Schall, S. Rodt, Z. Niu, N. Gregersen, S. Reitzenstein, and B. Munkhbat, “Assessing the Alignment Accuracy of State-of-the-Art Deterministic Fabrication Methods for Single Quantum Dot Devices,” *ACS Photonics*, vol. 11, pp. 1012–1023, Mar. 2024.
- [46] M. Galli, S. L. Portalupi, M. Belotti, L. C. Andreani, L. O’Faolain, and T. F. Krauss, “Light scattering and Fano resonances in high-Q photonic crystal nanocavities,” *Applied Physics Letters*, vol. 94, p. 071101, Feb. 2009.
- [47] X. Shang, B. Ma, H. Ni, Z. Chen, S. Li, Y. Chen, X. He, X. Su, Y. Shi, and Z. Niu, “C2v and D3h symmetric InAs quantum dots on GaAs (001) substrate: Exciton emission and a defect field influence,” *AIP Advances*, vol. 10, p. 085126, Aug. 2020.
- [48] C. Santori, D. Fattal, J. Vučković, G. S. Solomon, and Y. Yamamoto, “Indistinguishable photons from a single-photon device,” *Nature*, vol. 419, pp. 594–597, Oct. 2002.
- [49] A. Nick Vamivakas, Y. Zhao, C.-Y. Lu, and M. Atatüre, “Spin-resolved quantum-dot resonance fluorescence,” *Nature Physics*, vol. 5, pp. 198–202, Mar. 2009.
- [50] M. Von Helversen, A. V. Haisler, M. P. Daurtsev, D. V. Dmitriev, A. I. Toropov, S. Rodt, V. A. Haisler, I. A. Derebezov, and S. Reitzenstein, “Triggered Single-Photon Emission of Resonantly Excited Quantum Dots Grown on (111)B GaAs Substrate,” *physica status solidi (RRL)* – *Rapid Research Letters*, vol. 16, p. 2200133, Aug. 2022.
- [51] H. Wang, Y.-M. He, T.-H. Chung, H. Hu, Y. Yu, S. Chen, X. Ding, M.-C. Chen, J. Qin, X. Yang, R.-Z. Liu, Z.-C. Duan, J.-P. Li, S. Gerhardt, K. Winkler, J. Jurkat, L.-J. Wang, N. Gregersen, Y.-H. Huo, Q. Dai, S. Yu, S. Höfling, C.-Y. Lu, and J.-W. Pan, “Towards optimal single-photon sources from polarized microcavities,” *Nature Photonics*, vol. 13, pp. 770–775, Nov. 2019.
- [52] H. Ollivier, S. Thomas, S. Wein, I. M. De Buy Wenniger, N. Coste, J. Loredó, N. Somaschi, A. Harouri, A. Lemaitre, I. Sagnes, L. Lanco, C. Simon, C. Anton, O. Krebs, and P. Senellart, “Hong-Ou-Mandel Interference with Imperfect Single Photon Sources,” *Physical Review Letters*, vol. 126, p. 063602, Feb. 2021.
- [53] T. Legero, T. Wilk, A. Kuhn, and G. Rempe, “Time-resolved two-photon quantum interference,” *Applied Physics B*, vol. 77, pp. 797–802, Dec. 2003.
- [54] A. J. Brash and J. Iles-Smith, “Nanocavity enhanced photon coherence of solid-state quantum emitters operating up to 30 K,” *Materials for Quantum Technology*, vol. 3, p. 045001, Dec. 2023.
- [55] A. Schlehahn, S. Fischbach, R. Schmidt, A. Kagsanskiy, A. Strittmatter, S. Rodt, T. Heindel, and S. Reitzenstein, “A stand-alone fiber-coupled single-photon source,” *Scientific Reports*, vol. 8, p. 1340, Jan. 2018.
- [56] A. Musiał, K. Żołnaczyk, N. Srocka, O. Kravets, J. Große, J. Olszewski, K. Poturaj, G. Wójcik, P. Mergo, K. Dybka, M. Dyrkacz, M. Dłubek, K. Lauritsen, A. Bültner, P. Schneider, L. Zschiedrich, S. Burger, S. Rodt, W. Urbańczyk, G. Sęk, and S. Reitzenstein, “Plug&Play Fiber-Coupled 73 kHz Single-Photon Source Operating in the Telecom O-Band,” *Advanced Quantum Technologies*, vol. 3, p. 2000018, June 2020.
- [57] T. Gao, L. Rickert, F. Urban, J. Große, N. Srocka, S. Rodt, A. Musiał, K. Żołnaczyk, P. Mergo, K. Dybka, W. Urbańczyk, G. Sęk, S. Burger, S. Reitzenstein, and T. Heindel, “A quantum key distribution testbed using a plug&play telecom-wavelength single-photon source,” *Applied Physics Reviews*, vol. 9, p. 011412, Mar. 2022.
- [58] Q. Buchinger, S. Betzold, S. Höfling, and T. Huber-Loyola, “Optical properties of circular Bragg gratings with labyrinth geometry to enable electrical contacts,” *Applied Physics Letters*, vol. 122, p. 111110, Mar. 2023.
- [59] C. Ma, J. Yang, P. Li, E. P. Rugeramigabo, M. Zopf, and F. Ding, “Circular photonic crystal grating design for charge-tunable quantum light sources in the telecom C-band,” *Optics Express*, vol. 32, p. 14789, Apr. 2024.

- [60] L. Rickert, F. Betz, M. Plock, S. Burger, and T. Heindel, “High-performance designs for fiber-pigtailed quantum-light sources based on quantum dots in electrically-controlled circular Bragg gratings,” *Optics Express*, vol. 31, p. 14750, Apr. 2023.
- [61] S. Wijitpatima, N. Auler, P. Mudi, T. Funk, A. Barua, B. Shrestha, I. Limame, S. Rodt, D. Reuter, and S. Reitzenstein, “Bright electrically contacted circular Bragg grating resonators with deterministically integrated quantum dots,” June 2024. arXiv:2406.08057 [cond-mat, physics:physics].